7-1-2023

Evolution mechanism of grain orientation and texture distribution of Ti-6.5Al-3.5Mo-1.5Zr-0.3Si alloy under electroshocking treatment

Jian Zhou

Chang Liu

Yaya Wu

Lechun Xie

Fei Yin

See next page for additional authors

10.1016/j.jmrt.2023.07.028

Zhou, J., Liu, C., Wu, Y., Xie, L., Yin, F., Qian, D., . . . Hua, L. (2023). Evolution mechanism of grain orientation and texture distribution of Ti-6.5Al-3.5Mo-1.5Zr-0.3Si alloy under electroshocking treatment. Journal of Materials Research and Technology, 25, 5693-5704. https://doi.org/10.1016/j.jmrt.2023.07.028

Available online at www.sciencedirect.com

jmr&t
Journal of Materials Research and Technology

journal homepage: www.elsevier.com/locate/jmrt

Evolution mechanism of grain orientation and texture distribution of Ti-6.5Al-3.5Mo-1.5Zr-0.3Si alloy under electroshocking treatment

Jian Zhou [a,b], *Chang Liu* [a,b], *Yaya Wu* [a,b], *Lechun Xie* [a,b,*], *Fei Yin* [a,b], *Dongsheng Qian* [c], *Yanli Song* [a,b], *Liqiang Wang* [d], *Lai-Chang Zhang* [e], *Lin Hua* [a,b,**]

[a] *Hubei Key Laboratory of Advanced Technology for Automotive Components, Wuhan University of Technology, Wuhan, 430070, PR China*
[b] *Hubei Collaborative Innovation Center for Automotive Components Technology, Wuhan, 430070, PR China*
[c] *Hubei Engineering Research Center for Green Precision Material Forming, Wuhan University of Technology, Wuhan, 430070, China*
[d] *State Key Laboratory of Metal Matrix Composites, School of Materials Science and Engineering, Shanghai Jiao Tong University, No. 800 Dongchuan Road, Shanghai, 200240, PR China*
[e] *Centre for Advanced Materials and Manufacturing, School of Engineering, Edith Cowan University, 270 Joondalup Drive, Joondalup, Perth, WA, 6027, Australia*

ARTICLE INFO

Article history:
Received 23 May 2023
Accepted 3 July 2023
Available online 5 July 2023

Keywords:
Electroshocking treatment (EST)
Titanium alloy
Grain orientation
Texture distribution
Mechanical properties

ABSTRACT

It is well known that the mechanical properties of Ti-6.5Al-3.5Mo-1.5Zr-0.3Si are closely related to its microstructure and texture. In this work, a novel treatment of electroshocking treatment (EST) was adopted to optimize the microstructure and improve the mechanical properties of this titanium alloy. The grain orientation, texture, and mechanical properties of Ti-6.5Al-3.5Mo-1.5Zr-0.3Si alloy under EST were characterized and analyzed. With the increase of EST time to 0.04 s, the resultant acicular secondary α_s shows a tendency of spheroidization and the increase in grain diameter, which leads to a little decrease in hardness and yield strength. The increase in EST time to 0.06 s resulted in the precipitation of martensitic phases with high aspect ratios and a reduction in grain size in Ti-6.5Al-3.5Mo-1.5Zr-0.3Si alloy, as well as generating a more uniform texture distribution. The optimization of microstructure and texture significantly enhances the hardness and yield strength. The results in this work demonstrate that EST can serve as a novel method to regulate the microstructure and mechanical properties of Ti-6.5Al-3.5Mo-1.5Zr-0.3Si alloy.

* Corresponding author. Hubei Key Laboratory of Advanced Technology for Automotive Components, Wuhan University of Technology, Wuhan, 430070, PR China.
** Corresponding author. Hubei Key Laboratory of Advanced Technology for Automotive Components, Wuhan University of Technology, Wuhan, 430070, PR China.
E-mail addresses: xielechun@whut.edu.cn, lechunxie@yahoo.com (L. Xie), hualin@whut.edu.cn (L. Hua).
https://doi.org/10.1016/j.jmrt.2023.07.028

1. Introduction

Titanium alloys are extensively employed in a wide range of industries owing to their outstanding characteristics, including high specific strength, excellent corrosion resistance, and low density [1–5]. Ti-6.5Al-3.5Mo-1.5Zr-0.3Si is a typical dual-phase titanium alloy, consisting mainly of α and β phases. The mechanical and physical properties of Ti-6.5Al-3.5Mo-1.5Zr-0.3Si titanium alloy are closely related to its microstructure and crystal texture. Huang et al. [6] investigated the hot compression behavior and heat treatment effects of Ti-6.5Al-3.5Mo-1.5Zr-0.3Si at 995 °C and found that the tensile strength and elongation were significantly improved. Ouyang et al. [7] conducted an experiment to observe the grain growth conditions of Ti-6.5Al-3.5Mo-1.5Zr-0.3Si by isothermal β treatment within the temperature range of 1040 °C–1240 °C, and their findings suggested that the grain size increases with heating temperature and holding time. Zhang et al. [8] investigated the isothermal compression behavior of Ti-6.5Al-3.5Mo-1.5Zr-0.3Si within the temperature range of 1023 K–1323 K. The results revealed that the activation energy of deformation on the surface decreased with increasing strain. The optimization of the performance of Ti-6.5Al-3.5Mo-1.5Zr-0.3Si through heat treatment may require specific conditions such as high pressure, vacuum, and high temperatures. Hence, exploring simple, energy-efficient, and rapid methods for manipulating the microstructure is crucial for developing titanium alloys.

Electropulsing treatment is receiving more attention due to its short processing time and fast response speed [9–11]. Ben et al. [12] showed that the rapid modification of the microstructure and tensile properties of Ti-6.5Al-3.5Mo-1.5Zr-0.3Si by laser melting deposition, and their results showed that after electropulsing treatment, the initial heterogeneous microstructure transformed into a complete basketweave structure and heat-affected bands disappeared. Zhang et al. [13] investigated the electroplastic compression behavior of Ti–6Al–4V alloy and significant changes occurred in the mechanical properties of Ti–6Al–4V under the influence of high-energy pulse current. Electroshocking treatment (EST) has more advantages compared to electropulsing treatment, such as being instantaneous, efficient, and having a fast response time. Xie et al. [14–16] studied the influence of EST on Ti–5Al–5Mo–5V–3Cr–1Zr produced by laser melting deposition. The results indicated that the α phase tended to

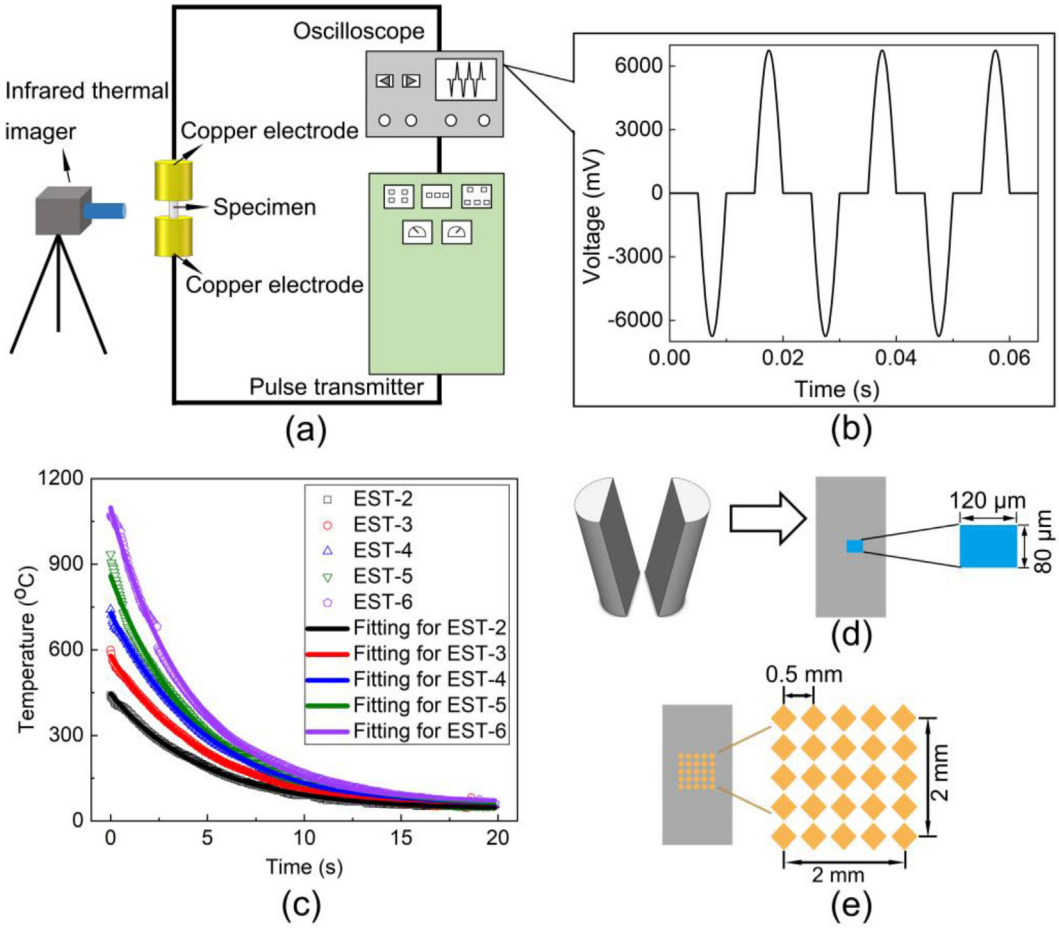

Fig. 1 – Schematic diagram of the experimental apparatus and specimen preparation procedure: (a) experimental apparatus, (b) EST pulse waveform, (c) the maximum temperature curve of the specimen surface monitored by the infrared thermal imager, (d) electrical Discharge Machining (EDM) cutting and EBSD characterization area, (e) hardness measurement area and the distance between two test position.

precipitate along the grain boundaries. Furthermore, an increase in the radius of curvature at the α tip was accompanied by a significant spheroidization phenomenon. Song et al. [17] studied the fatigue life of Ti-6.5Al-3.5Mo-1.5Zr-0.3Si using the EST method, and their experimental results showed that, by properly adjusting the EST parameters, the low cycle fatigue life could be increased by 22.5%. Liu et al. [18–20] found that the transformation from secondary α phase (α_s) to β phase, along with the precipitation of acicular α phase after EST, which significantly determine the mechanical properties of Ti-6.5Al-3.5Mo-1.5Zr-0.3Si. As such, the advantage of EST can be used to optimize the microstructure and mechanical properties of Ti-6.5Al-3.5Mo-1.5Zr-0.3Si alloy, which can provide new ideas and methods for efficient, energy-saving, and reliable to manufacturing titanium alloys.

In this work, the evolution of phase structure, grain size, grain boundary, and texture of Ti-6.5Al-3.5Mo-1.5Zr-0.3Si were characterized using scanning electron microscopy (SEM) and electron back-scattered diffraction (EBSD) techniques for different EST. Finally, the effect of EST on the hardness was analyzed. The expected results would provide both a more comprehensive understanding of the microstructural evolution in Ti-6.5Al-3.5Mo-1.5Zr-0.3Si and guidance for future processing and optimization.

2. Experimental

2.1. Specimen preparation and experimental procedure

The as-received Ti-6.5Al-3.5Mo-1.5Zr-0.3Si alloy was cut into cylinders with a diameter of 5 mm and a length of 10 mm using electrical discharge machining (EDM) method. The specimen surface was polished with sandpaper prior to conducting EST. The EST equipment mainly consisted of a pulse transmitter, an oscilloscope, and copper electrodes, with the specimen being placed between two copper electrodes, as shown in Fig. 1(a). The pulse transmitter was utilized to generate a pulse waveform with a period of 0.02 s (Fig. 1(b)), and the amplitude of the pulse waveform was measured as 4200 A by Hall current sensor. An oscilloscope was employed for real-time monitoring of pulse signals. The EST time for each specimen and their corresponding specimen number are shown in Table 1, Meanwhile, an infrared thermal imager was used to monitor the temperature data of the specimen surface (Fig. 1(c)).

Table 1 – The processing parameters and mechanical properties after EST.

Specimen number	EST time (s)	grain equivalent diameter D_a (μm)	Yield strength (MPa)	Fracture strain (%)
EST-0	0	1.62	968 ± 11	34.9 ± 0.86
EST-2	0.02	1.64	972 ± 9	35.1 ± 1.21
EST-3	0.03	1.63	958 ± 14	39.4 ± 1.52
EST-4	0.04	1.75	948 ± 21	33.4 ± 1.85
EST-5	0.05	1.46	1250 ± 12	22.5 ± 1.14
EST-6	0.06	1.48	1518 ± 18	21.5 ± 0.98

2.2. Microstructure characterization

The specimens were cut along their central axes using the EDM method (Fig. 1(d)). Subsequently, the specimens were mechanically ground using sandpapers. Finally, the specimens were polished using a mixture of silica suspension and H_2O_2 (V_{SiO2}:V_{H2O2} = 3:2). The phase structure and grain orientation were characterized using a JEOL IT800 SEM with an Oxford C-Nano EBSD system, operating at a voltage of 15 kV and a working distance of 10 mm. The scanning step for EBSD characterization was set to 0.2 μm, with a scanning area of 120 μm × 80 μm located in the central region of specimen (Fig. 1(d)). The Matlab 2021b software toolbox was utilized for the processing of EBSD data and texture analysis [21–23]. The Vickers hardness tester (HV-1000A, Huayin LLC, China) was employed to measure the hardness in the central region of the specimen (Fig. 1(e)). The positions of hardness measurement were arranged in a 5 × 5 matrix with 0.5 mm between each two adjacent points (Fig. 1(e)). A load of 500 N was applied with the dwell time of 5 s during hardness test. The compression fracture behavior of the specimen was performed at room temperature using the SANS-CMT5205 compression testing machine. The compression rate was set at 0.05 mm/min. The compressed specimen had a cylindrical shape with a diameter of 5 mm and a length of 10 mm.

3. Results and discussion

3.1. Evolution of phases structure

Fig. 2 illustrates the phase variation under different EST time using Backscattered Electron Diffraction (BED) model. From Fig. 2 (a) and (b), the initial phases are equiaxed structure, which mainly contains primary α phase (α_p), α_s and β phase. The phases are distributed along the horizontal direction due to forging process (Fig. 2(a)). From the magnified image in Fig. 2(a), the acicular α_s phase is dispersed within the β phase (Fig. 2(b)). After EST with 0.02 s and 0.03 s, the acicular α_s phase shows a trend of gradual decreasing in quantity and shortening in shape (Fig. 2(d) and (f)). With the increase in EST time, the α_s phase transforms to β phase, the quantity of the acicular α_s phase decreases (Fig. 2(h) and (j)). This phenomenon is caused by high-energy electric current, which leads to a phase transformation from the acicular α_s to β. Previous literature indicated the phase transition from α_s phase to β phase [19]. Due to the higher energy at the tip of α_s, the phase transition process first occurs at the tip and gradually spreads from the tip to the central region, causing α_s phase to show a tendency of spheroidization (Fig. 2(f)). When the energy continuously increases, the central region of the α_s phase would also undergo a complete phase transition and transform entirely into the β phase, causing a reduction in the number of α_s phase (Fig. 2(h), (j) and (l)).

In specimen EST-0, the α_p phase with a high aspect ratio is uniformly distributed mainly along the horizontal direction (Fig. 2(a) and (b)), because the high temperature induced by EST would also promote the transformation of α_p phase to β phase (Fig. 1(c)), resulting in a slight increase in β phase

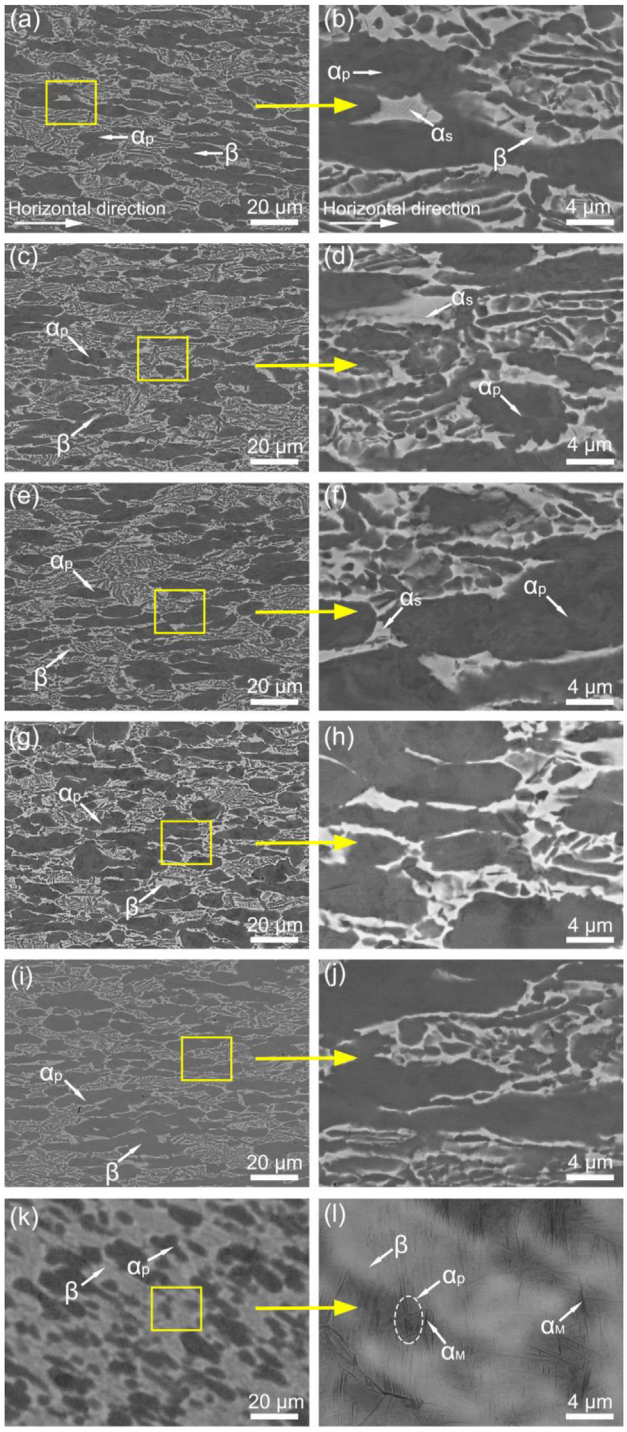

Fig. 2 – Phase structure before and after EST: (a) and (b) EST-0; (c) and (d) EST-2; (e) and (f) EST-3; (g) and (h) EST-4; (i) and (j) EST-5; (k) and (l) EST-6; And (b), (d), (f), (h), (j), (l) are magnified images that are marked by rectangular regions.

content (Fig. 2(i)). Meanwhile, the shape of α_p exhibits a trend of gradual approaching spherical shape from high aspect ratio to low aspect ratio (Fig. 2(g)). In the air cooling condition, a rapid increase in temperature can alter the original phase transition process, causing a transformation from the α_p phase to the martensitic phase α_M instead of the β phase. Further observation shows that, compared with the EST-0, the alternating distribution of α_p phase and β phase is more uniform. At the same time, the martensite phase α_M is mainly concentrated around the α_p phase, and a few martensite phase α_M is observed within the β phase (white), as shown in Fig. 2(l).

3.2. *Grain size and grain orientation*

Fig. 3 shows the grain orientation. In EST-0, the large grains distributed along the rolling direction (RD) direction exhibit a significant preferred orientation distribution in Fig. 3(a), with a strong orientation along the <0001 > direction. By contrast, after EST, the size and color diversity of large-sized grains are increased, which implies that EST promotes the anisotropy of orientation. Large-size grains exhibit strong orientation along the <−12-10 > and <−1100 > directions, as shown in Fig. 3(e). To further investigate the effect of EST on grain size variation, the grain size distribution is shown in Fig. 4. For each grain, its grain equivalent diameter D and its distribution can be defined as [24]:

$$S = \pi^{*}(D/2)^2 \tag{1}$$

$$f(D,\mu,\sigma) = \frac{1}{D\,\sigma\sqrt{2\pi}} exp\left[-\frac{1}{2\sigma^2}(\ln D - \mu)^2\right] \tag{2}$$

where S is the area of the grain, which is determined by the total number of pixels inside grain; π is a constant. The distribution of grain equivalent diameter is fitted using a lognormal distribution $f(D, \mu, \sigma)$, where μ represents the mean value and σ represents the standard deviation. In Fig. 4, the average grain equivalent diameter D_a reaches 1.62 μm in EST-0. With the increase of EST time, the temperature of the specimen surface increases (Fig. 1(c)), and the thermal effect and athermal effect are induced by the current, leading to an increase in grain equivalent diameter, as shown in Fig. 4(b)–(d). In EST-2, EST-3, and EST-4, the D_a are 1.64 μm, 1.63 μm, and 1.75 μm, respectively. By contrast, the increase in EST time results in the reduction of D_a. As illustrated in Fig. 4(e) and (f), with the increase of EST time to 0.05 s and 0.06 s, D_a decreases to 1.46 μm and 1.48 μm, respectively. Compared to EST-0 (Fig. 4(a)), the standard deviation μ of EST-5 and EST-6 decreases from 1.62 to 1.46 and 1.48 (Fig. 3(e) and (f)), respectively, which implies a more uniform distribution of grain diameters after EST [25].

Fig. 5(a) shows the profile of grain A, which is the maximum grain area shown in Fig. 3(a). In order to better illustrate the morphology of grains, the aspect ratio of grain, denoted as $GS(i)$, can be described as Eq. (3) [26]:

$$GS(i) = \frac{P}{E_p} \tag{3}$$

where E_p is the equivalent perimeter, which is calculated by grain equivalent diameter D. P is the perimeter, which is determined by the total number of pixels along the grain boundary, and i is the grain number.

When all grains are considered, the average values of grain shape are shown in Fig. 5(b), which exhibits a trend of exponential growth, especially for EST-6 specimen. The shape

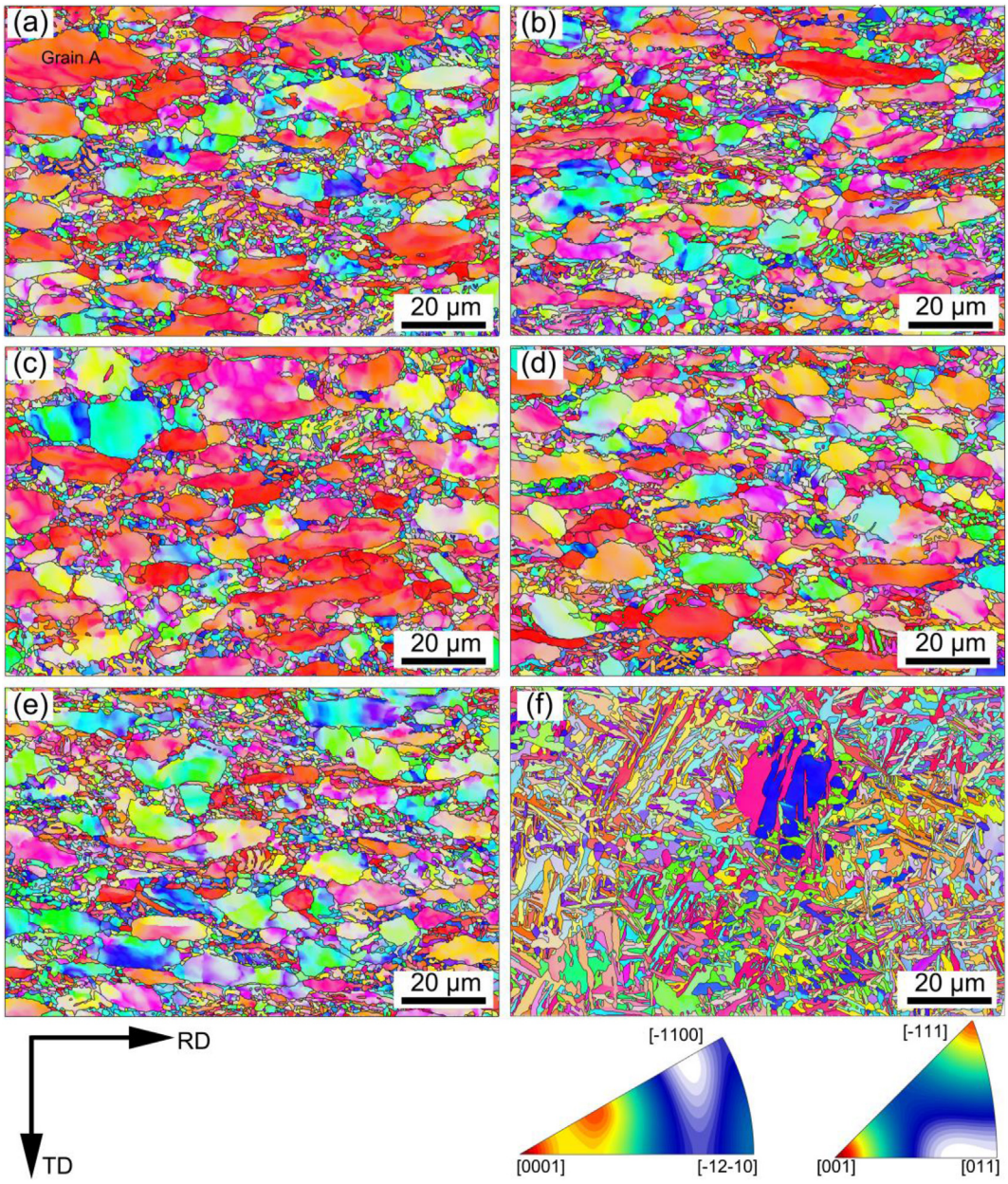

Fig. 3 – Grain orientation of specimens (a) EST-0, (b) EST-2, (c) EST-3, (d) EST-4, (e) EST-5, (f) EST-6.

factor *GS* reaches 1.39. The increase of GS in EST-6 indicates that it is mainly composed of grains with high aspect ratio. This is consistent with the abundance of acicular martensite α_M observed in Fig. 2(l). In addition, the grain boundary is not smooth and shows a wave-shape at the pixel level, as shown in Fig. 5(a). These results indicate the uncertain direction of grain boundary migration, especially for medium and large angle grains boundary, the directions of grain boundary migration are quite limited [27–29]. In other words, after EST with 0.06 s, the migration of grain boundary migration becomes more ordered, resulting in the precipitation of α_M phase with a high aspect ratio. As such, the GS value increases (Fig. 5(a)).

3.3. *Grain boundary and orientation variation*

Fig. 6(a)–(l) shows the distribution and statistics of misorientation angle of specimens under different EST time. It is well accepted that, the grain boundaries mostly consist of low-angle grain boundaries (LAGBs) ($2° \leq$ LAGBs$\leq 15°$) and high-angle grain boundaries (HAGBs) (HAGBs$>15°$). Here the black lines are marked with the HAGBs, and the LAGBs in α phase and β phase are depicted as turquoise and blue lines, respectively. As observed from Fig. 6 (a), the HAGBs (black lines) is dominant in EST-0. Meanwhile, the LAGBs (turquoise lines) are randomly and uniformly distributed within the α grains. Further, the HAGBs are distributed along the periphery of the

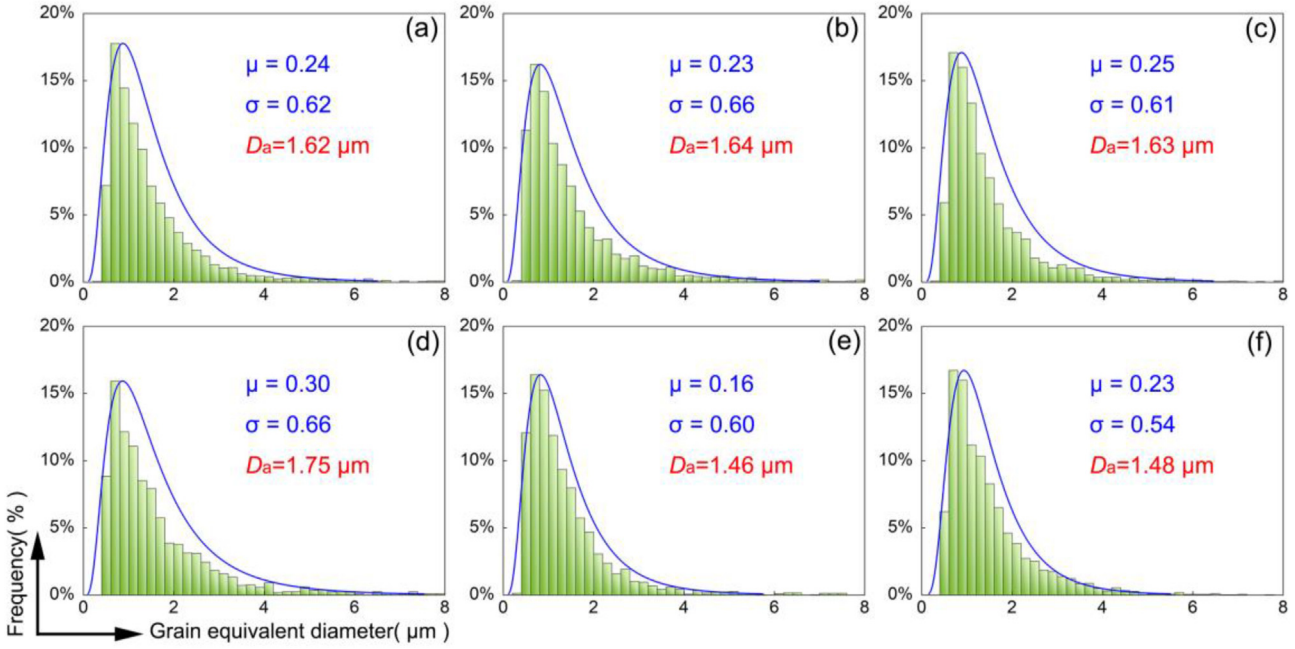

Fig. 4 – Grain size distribution of specimens under different EST time (a) EST-0, (b) EST-2, (c) EST-3, (d) EST-4, (e) EST-5, (f) EST-6. Here, D_a represents the average value of grain equivalent diameter, μ and σ represent the mean and standard deviation of the lognormal distribution fitting curve, respectively.

grains, typically independent of crystallographic misorientation, while the LAGBs are mainly evenly distributed inside the α grains and β grains (Fig. 6(a)–(f)). This may indicate that the interior of the intact grain is abundant of subgrains and dislocations, which is likely to cause dislocation slip with twinning [30]. However, the decrease of the turquoise lines in Fig. 6 (f) indicates that the high-density current can promote the migration of LAGBs within the β grains. Fig. 6(g)–(l) shows the misorientation angle histogram. In Fig. 6(a), LAGBs exhibit a prominent preferential misorientation angle, and the peak value of misorientation angle about 2° and the proportion of HAGBs is 30.93%. This indicates the existence of a certain quantity of deformed grains. When the EST time increases, the proportion of HAGBs decreases to 20.85%, 20.23%, 22.08%, and 23.23% in EST-2, EST-3, EST-4, and EST-5, respectively. But there is no significant variation in the peak misorientation angle. This phenomenon can be attributed to the coupled effects of thermal and athermal effect induced by electric currents, which facilitates the migration of grain boundary and the growth of grain [31]. Notably, the percentage of HAGBs exhibits a sharp increase to 88.62% for EST-6. Simultaneously, the peak deviation of the misorientation angle distribution is evident, with a value of 60° in Fig. 6(l). This indicates that the prolonged effect of current would be more beneficial in promoting the migration of LAGBs compared to HAGBs.

The kernel average misorientation (KAM) serves as a quantitative characterization of the local grain misorientation and reflects the local stress distribution and energy storage value [32]. The $KAM_{i,j}$ at pixel (i, j) can be defined as:

$$KAM_{i,j} = \frac{1}{|N(i,j)|} \sum_{(k,l)\in N(i,j)} w\left(o_{0,k,l}, o_{0,i,j}\right) \quad (4)$$

Here, $w(o_{0,k,l}, o_{0,i,j})$ represent the disorientation angle between the central pixel orientation $o_{0,i,j}$ and its neighboring pixel orientation $o_{\Phi,k,l}$, Φ is the kernel size of consideration for neighbor order pixel N(i, j) is the set of all neighboring pixels.

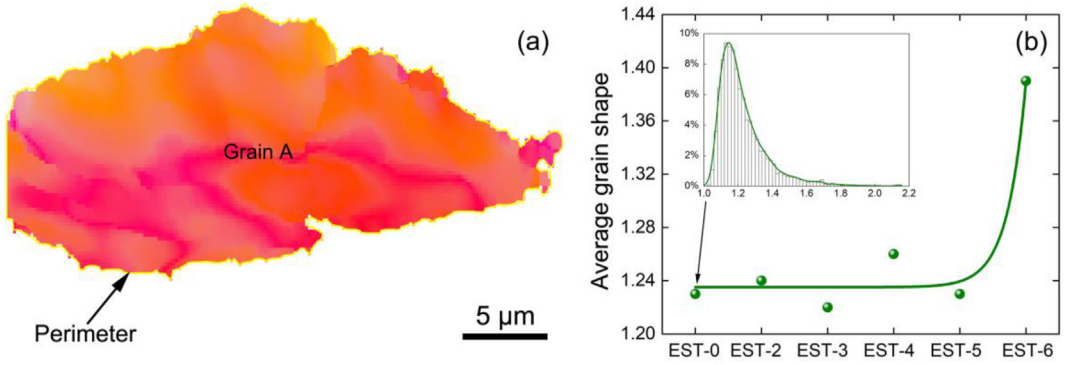

Fig. 5 – (a) Grain shape measurement method, (b) average grain shape for different EST process.

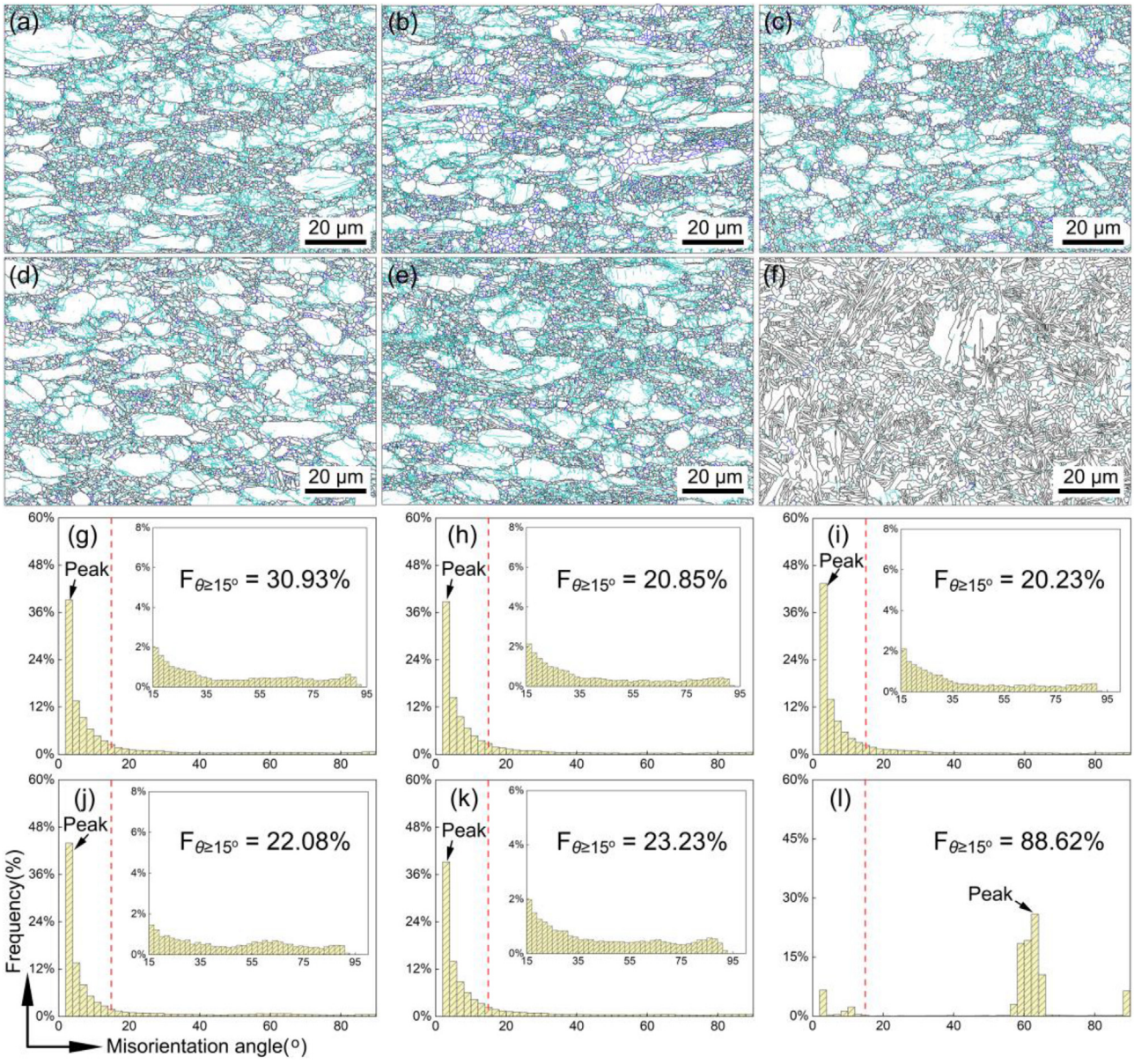

Fig. 6 – Misorientation angle distribution of specimens: (a) EST-0, (b) EST-2, (c) EST-3, (d) EST-4, (e) EST-5, (f) EST-6. Statistics of misorientation angle of specimens: (g) EST-0, (h) EST-2, (i) EST-3, (j) EST-4, (k) EST-5, (l) EST-6.

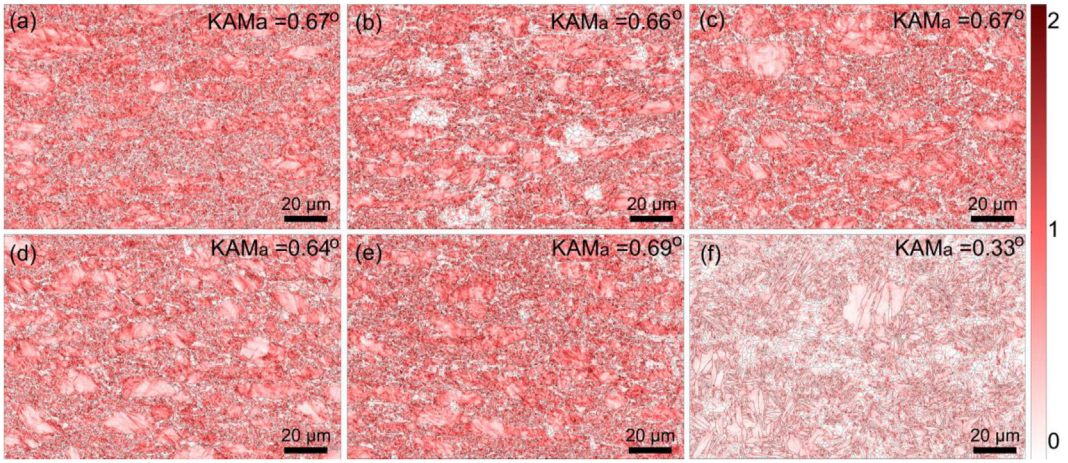

Fig. 7 – Kernel average misorientation (KAM) of specimens: (a) EST-0, (b)EST-2, (c) EST-3, (d) EST-4, (e) EST-5, (f) EST-6.

In order to ensure the accuracy of calculation, the value of Φ in this work was set to 1 based on Matlab software [33]. The average value of KAM (KAM_a) for each specimen can be expressed as:

$$KAM_a = \frac{1}{m*n} \sum_{(i,j)\in(m,n)} KAM_{i,j} \quad (5)$$

where (m,n) is the set of EBSD characterization pixels; here, $m = 600$, $n = 400$. Fig. 7 displays the KAM distribution of different specimens, which demonstrates that KAM distributes homogeneously within the grain and near the grain boundary. Compared to the EST-0 ($KAM_a = 0.67°$), the KAM_a value of the specimen remain essentially invariant by electric current in a short time. The KAM_a values for EST-2, EST-3, EST-4 and EST-5 are 0.66°, 0.67°, 0.64° and 0.69° (Fig. 7(a)–(e)), respectively. As further increase in EST time, the KAM value is reduced (Fig. 7(f)). These results indicate that, for EST-6, a significant amount of martensite precipitation has taken place, and the orientation distribution of the grain become more uniform [34].

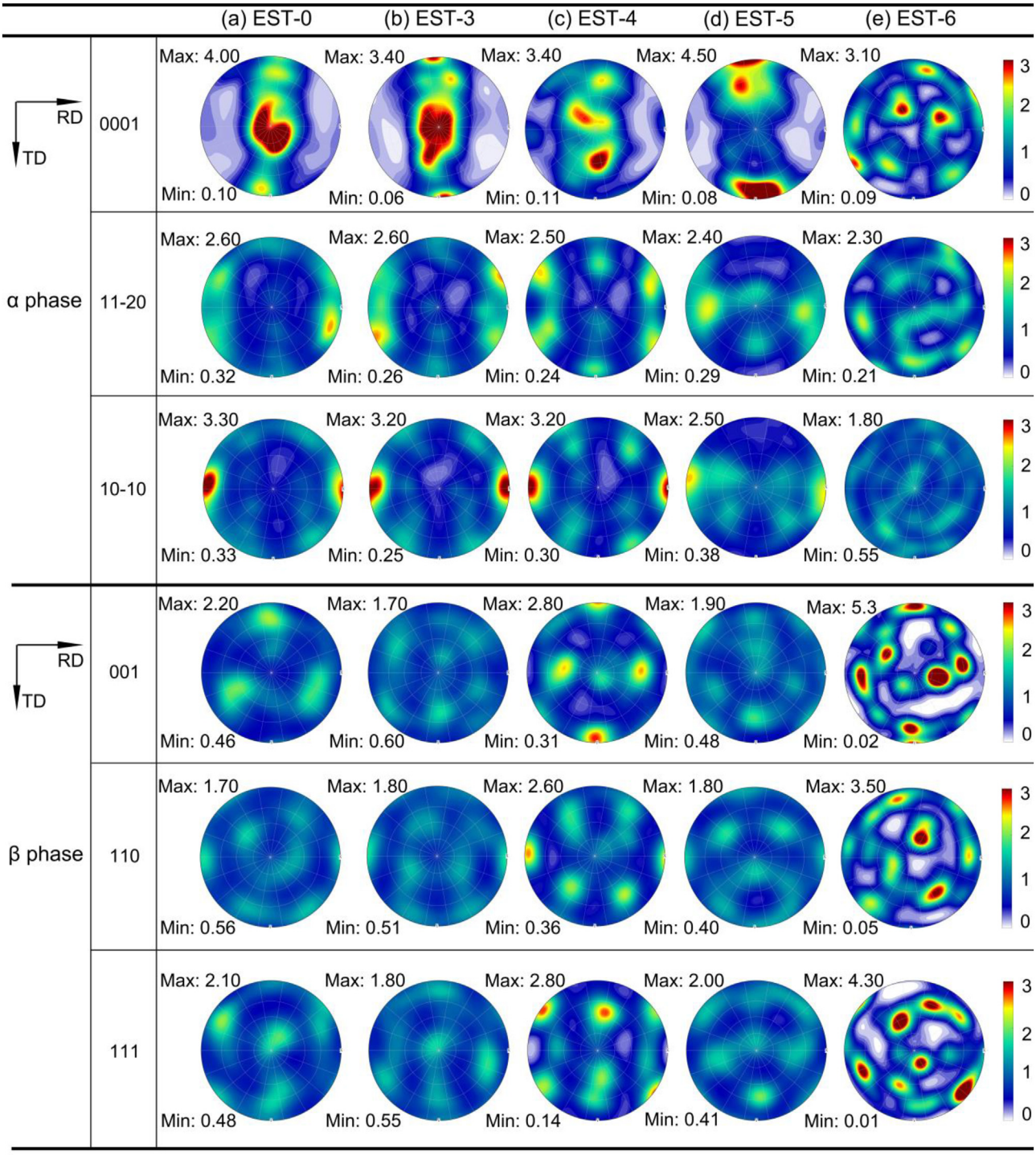

Fig. 8 – Pole figures of specimens under different EST time.

3.4. *Texture evolution*

To investigate the texture distribution in more detail, Fig. 8 displays the pole figures in the central region of specimens. For EST-0 specimen, both the α phase and β phase texture directions exhibit high symmetry along the Z-axis (Fig. 8(a)). Compared to the β phase, the α phase exhibits more preferred orientations and higher texture intensity along (0001) direction. In terms of texture intensity, the maximum texture intensity of the α phase (0001) is 4, with a bunch of strong intensity in the normal direction (ND). With the increase of EST time, the texture intensity of α phase along the (0001) direction shows a decreasing trend except for EST-5 (Fig. 8(a)–(e)). In contrast, the texture intensity of the α phase along the (11–20) direction is independent of the EST process. However, for α phase (10-10), the maximum texture intensity decreases continuously (Fig. 8(a)–(e)). This result further indicates that, after EST, there is a significant preferred crystallographic orientation in the grain orientation distribution. EST also has an important effect on the β phase texture intensity; especially in EST-6, its texture intensity in the three directions of (001), (110) and (111) increase significantly (Fig. 8(e)). This is due to when the temperature exceeds the phase transition temperature, the α phase will transform into the β phase [35–37]. The orientation obeys the Burgers relationship of $(110)_\beta//(0001)_\alpha$ and $[111]_\beta//[11\bar{2}0]_\alpha$ [38].

Furthermore, evaluating from the perspective and peak quality of texture distribution, the EST can significantly enhance the distribution of crystal orientation diversity, and in specific texture directions, the quantity of strongest peaks shows a trend of continuous increase, such as in the α phase along (0001) direction (Fig. 8(a)–(e)). The EST-6 shows the quantity of highest intensity peaks splitting from one to three compared to the EST-0 (Fig. 8(a)). This phenomenon is more pronounced in the β phase, the quantity of the strongest texture peaks in the directions of (001), (110), and (111) are 6, 3, and 7 (Fig. 8(e)), respectively. Additionally, the Maximum texture intensity exhibits near axis rotational symmetry after EST-6 (Fig. 8(e)). These results show that EST contributes to the uniformity of texture distribution, which could effectively improve mechanical properties. This will be discussed in the following section.

3.5. *Mechanical properties*

Fig. 9 presents the hardness measurements for different EST process parameters. Basically, the average hardness values of EST-0, EST-2, EST-3, EST-4, EST-5, and EST-6 are approximately 316 HV, 318 HV, 306 HV, 305 HV, 329 HV, and 354 HV, respectively. Appropriate EST intensity contributes to the growth and enlargement of grains [39]. With the increase in EST time, the hardness exhibits a discernible trend of initially decreasing slightly followed by subsequent increasing. Further analysis revealed that the variation trend of hardness coincides with the variation pattern of grain average diameter (Fig. 4). In general, there exist four distinct mechanisms for hardening of metals, including precipitation hardening, grain boundary hardening, dislocation hardening, and solid solution hardening (the predominant interstitial elements comprise of oxygen and nitrogen) [40,41]. One hand, fine martensitic phases α_M are precipitated after EST-5 and EST-6 (Fig. 2(k)–(l)), which are uniformly distributed around the α phase, and the α_M is harder than the β phase. On the other hand, the increase in the number of grain boundaries hinders the movement of dislocations, which has a positive effect on the improvement of hardness. Therefore, the increase of hardness can be attributed to the combined effects of grain boundary hardening and precipitation hardening. Meanwhile, we observe that the EST-6 exhibits a smaller hardness error bar (Fig. 9), which may be caused by the more homogeneous texture distribution and the more uniform grain size distribution.

Fig. 10 shows the compressive stress-strain curves of specimens after different EST treatment time. In EST-0, the yield stress and fracture strain are 968 MPa and 34.9%, respectively. With EST time of 0.02 s, no significant changes in yield stress and fracture strain are noted. However, after EST time of 0.03 s and 0.04 s, the yield stress of EST-3 and EST-4 vary slightly as 958 MPa and 948 MPa, while the fracture

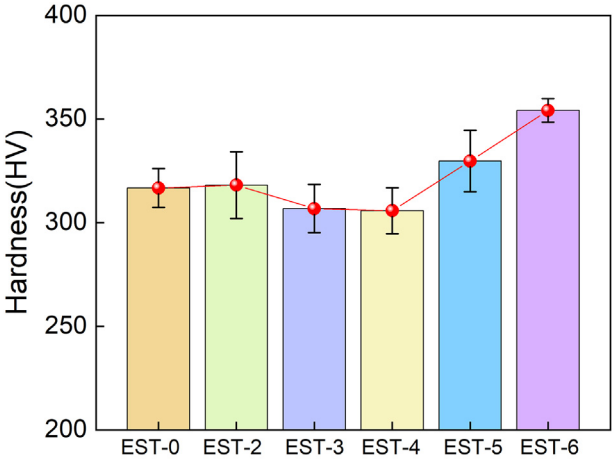

Fig. 9 – Hardness average value under different conditions.

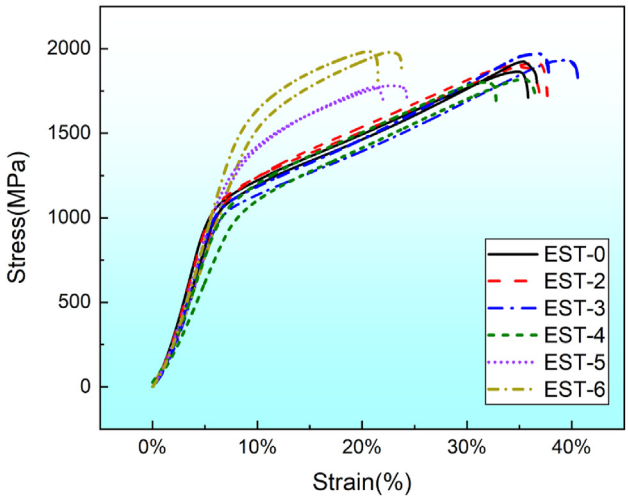

Fig. 10 – Compressive stress - strain curves of EST-0, EST-2, EST-3, EST-4, EST-5 and EST-6.

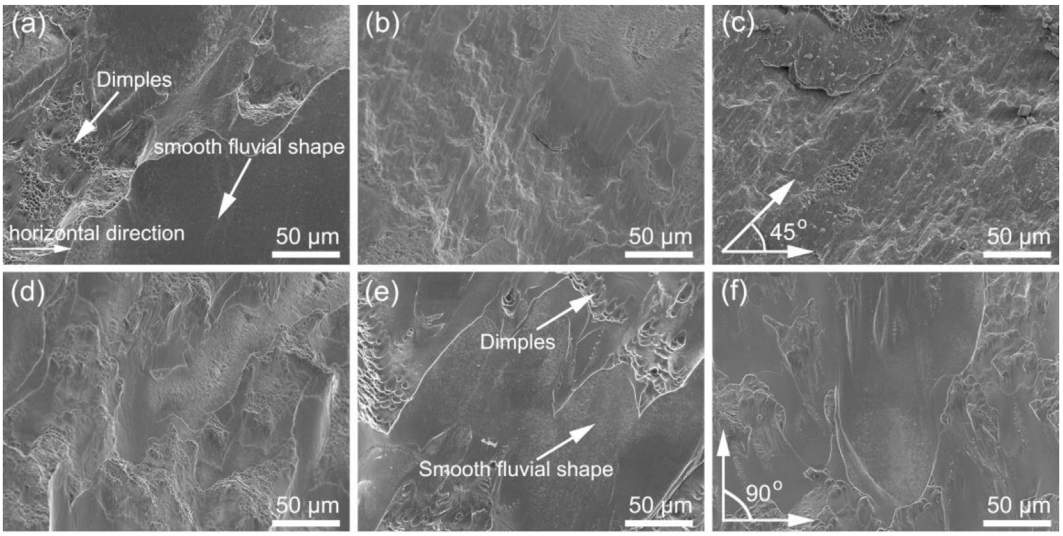

Fig. 11 – Compression fracture morphology of specimens (a) EST-0, (b) EST-2, (c) EST-3, (d) EST-4, (e) EST-5, (f) EST-6.

strain are 39.4% and 33.4%, respectively. Further increasing the EST time to 0.05 s and 0.06 s, according to the Hall-Patch relationship, the yield stress of metal increases with decreasing grain diameter D [42,43], EST-5 and EST-6 with smaller grain diameters have larger yield strength (Fig. 4), which are 1250 MPa and 1518 MPa, respectively. At the same time, those alloys with finer grains have more grain boundaries, which restrict the movement of dislocations and result in a decrease in fracture strain [44,45]. As shown in Fig. 10, the fracture strains of EST-5 and EST-6 decrease to 22.5% and 21.5%. The yield strength and fracture strain are summarized in Table 1.

In order to further analyze the compression fracture behavior, Fig. 11 shows the compression fracture morphology of specimens with different EST time. For EST-0 (Fig. 11(a)), the fracture morphology is mainly composed of two characteristics: dimples and smooth fluvial shape, which represent the plastic fracture mode and the brittle fracture mode [46,47], respectively. After EST with 0.02 s, 0.03 s and 0.04 s, the fracture morphology shows an increase in rough stepped platform, this implies that EST-2, EST-3 and EST-4 samples are dominated by plastic fracture (Fig. 11(b), (c), (d)). However, after the EST time of 0.05 s and 0.06 s, the amount of smooth and flat surface significantly increases, indicating that the EST-5 and EST-6 specimens are mainly brittle fracture (Fig. 11(e), (f)). Generally, the specimen could fracture along its maximum stress direction, as shown in Fig. 11. The deformation direction of EST-0, EST-2, EST-3, and EST-4 are 45° from the horizontal direction, while the deformation direction of EST-6 is closely parallel to the vertical direction, the vertical direction is parallel to the direction of the applied load. This phenomenon indicates that high-energy pulse current can optimize the stress distribution inside the specimen and promote it transition from plastic fracture to brittle fracture [48,49]. All results indicate that EST can modify the microstructure effectively and improve the mechanical properties at sub-second time.

4. Conclusions

In this work, the microstructure variation, texture evolution and mechanical properties of Ti-6.5Al-1.5Zr-3.5Mo-0.3Si titanium alloy under EST were investigated. Some important results were obtained.

(1) Before EST, the material consisted of the α_p phase, α_s phase, and β phase. After EST with 0.02 s, 0.03 s, and 0.04 s, the quantity of α_s phase gradually decreased, and its shape tended to become more spherical. Further increase in the EST time, martensitic α_M phase precipitated around the α_p phase, which was mainly attributed to the effect of the thermal and athermal effects caused by EST.
(2) After EST with 0.02 s, 0.03 s, and 0.04 s, the equivalent grain diameter D_a continued to increase. Increasing the EST time to 0.05 s and 0.06 s, the D_a decreased and the grains were distributed more uniformly. The shape of grains was gradually elongated with a high length-width ratio, and the anisotropy of the orientation became apparent.
(3) After EST with 0.06 s, the texture intensity of α phase decreased while β phase increased, and the texture distribution of α phase and β phase was more uniform. After EST with 0.02 s, 0.03 s, and 0.04 s, the hardness slightly decreased. However, after EST with 0.05 s and 0.06 s, the hardness increased, which was ascribed to the precipitation of martensitic α_M phase and the significant increase in the number of HAGBs.
(4) After EST with 0.02 s, 0.03 s, and 0.04 s, the compression experiments results indicated that the fracture mode exhibited both plastic fractures and brittle fractures, and the yield strength slightly changed while the fracture strain increased. After EST with 0.05 s and 0.06 s, the brittle fracture dominated, and the yield strength increased while the fracture strain decreased. The improvement of yield strength was ascribed to the

precipitation of α_M phase and the increase in the number of grain boundaries, which could hinder the movement of dislocations and benefit its mechanical properties.

All results show that EST is an effective approach for tailoring the microstructure and mechanical properties of titanium alloys.

Contribution of each author

Jian Zhou: Investigation, Data curation, Writing - original draft.
Chang Liu and Yaya Wu: Writing - review & editing.
Lechun Xie: Methodology, Writing - original draft, Writing - review & editing.
Fei Yin: Writing - review & editing.
Dongsheng Qian: Writing - review & editing.
Yanli Song: Writing - review & editing.
Liqiang Wang: Writing - review & editing.
Lai-Chang Zhang: Writing - review & editing.
Lin Hua: Supervision, Methodology, Writing - review & editing.

Data availability

The raw/processed data required to reproduce these findings cannot be shared at this time as the data also forms part of an ongoing study.

Declaration of competing interest

The authors declare that they have no known competing financial interests or personal relationships that could have appeared to influence the work reported in this paper.

Acknowledgements

This work was financial supported by National Natural Science Foundation of China (Grant No. 51975441, No. 52271135), Major Research Plan of the National Natural Science Foundation of China (Grant No. 92266102), Natural Science Foundation of Hubei Province (Grant No. 2022CFB492), Knowledge Innovation Program of Wuhan -Basic Research (No. 2022010801010174), Innovation Funding Project of National Engineering and Research Center for Commercial Aircraft Manufacturing (COMAC-SFGS-2022-1871), "Chu Tian Scholar" project of Hubei Province (CTXZ2017-05), Overseas Expertise Introduction Project for Discipline Innovation (B17034) and Innovative Research Team Development Program of Ministry of Education of China (IRT_17R83).

Appendix A. Supplementary data

Supplementary data to this article can be found online at https://doi.org/10.1016/j.jmrt.2023.07.028.

REFERENCES

[1] Bazaka O, Bazaka K, Truong VK, Levchenko I, Jacob MV, Estrin Y, et al. Effect of titanium surface topography on plasma deposition of antibacterial polymer coatings. Appl Surf Sci 2020;521:146375.
[2] Kazek-Kęsik A, Nosol A, Płonka J, Śmiga-Matuszowicz M, Student S, Brzychczy-Włoch M, et al. Physico-chemical and biological evaluation of doxycycline loaded into hybrid oxide-polymer layer on Ti–Mo alloy. Bioact Mater 2020;5(3):553–63.
[3] Mohammed MT, Khan ZA, Geetha M, Siddiquee AN. Microstructure, mechanical properties and electrochemical behavior of a novel biomedical titanium alloy subjected to thermo-mechanical processing including aging. J Alloys Compd 2015;634:272–80.
[4] Semenova IP, Polyakov A, Polyakova VV, Grishina YF, Huang Y, Valiev RZ, et al. Mechanical behavior and impact toughness of the ultrafine-grained Grade 5 Ti alloy processed by ECAP. Mater Sci Eng, A 2017;696:166–73.
[5] Zhang LC, Chen LY. A review on biomedical titanium alloys: recent progress and prospect. Adv Eng Mater 2019;21(4):1801215.
[6] Huang L, Geng L, Li A, Wang G, Cui X. Effects of hot compression and heat treatment on the microstructure and tensile property of Ti–6.5 Al–3.5 Mo–1.5 Zr–0.3 Si alloy. Mater Sci Eng, A 2008;489(1–2):330–6.
[7] Ouyang D-L, Du H-M, Cui X, Lu S-Q, Dong X-J. Grain growth behavior of Ti–6.5 Al–3.5 Mo–1.5 Zr–0.3 Si alloy during isothermal β heat treatments. Rare Met 2019;38:233–7.
[8] Zhang X, Li M, Li H, Luo J, Su S, Wang H. Deformation behavior in isothermal compression of the TC11 titanium alloy. Mater Des 2010;31(6):2851–7.
[9] Li YY, Ma SY, Liu CM, Zhang M. Microstructure and mechanical properties of Ti-6.5 Al-3.5 Mo-1.5 Zr-0.3 Si alloy fabricated by arc additive manufacturing with post heat treatment, key engineering materials. Trans Tech Publ; 2018. p. 161–9.
[10] Pan D, Zhao Y, Xu X, Wang Y, Jiang W, Ju H. Effect of high-energy and instantaneous electropulsing treatment on microstructure and propertiesof 42CrMo steel. Acta Metall Sin 2018;54(9):1245–52.
[11] Zhao Z, Wang G, Hou H, Han B, Zhang Y, Zhang N. Influence of high-energy pulse current on the mechanical properties and microstructures of Ti-6Al-4V alloy. J Mater Eng Perform 2017;26:5146–53.
[12] Ben D, Yang H, Gao J, Yang B, Dong Ya, Liu X, et al. Rapid microstructure homogenization of a laser melting deposition additive manufactured Ti-6.5 Al-3.5 Mo-1.5 Zr-0.3 Si alloy by electropulsing. Materials 2022;15(20):7103.
[13] Zhang J, Liu Z, Sun J, Zhao H, Shi Q, Ma D. Microstructure and mechanical property of electropulsing tempered ultrafine grained 42CrMo steel. Mater Sci Eng, A 2020;782:139213.
[14] Xie L, Guo H, Song Y, Liu C, Wang Z, Hua L, et al. Effects of electroshock treatment on microstructure evolution and texture distribution of near-β titanium alloy manufactured by directed energy deposition. Mater Char 2020;161:110137.
[15] Wen Y, Liu P, Guo H, Tian L, Wang L, Wang Z, et al. Effect of electroshocking treatment on the microstructure and mechanical properties of laser melting deposited near-β Ti-55531 thin-wall. J Alloys Compd 2023;936:168187.
[16] Xie L, Guo H, Song Y, Hua L, Wang L, Zhang L-C. Novel approach of electroshock treatment for defect repair in near-β titanium alloy manufactured via directed energy deposition. Metall Mater Trans 2021;52:457–61.

[17] Song Y, Wang Z, Yu Y, Wu W, Wang Z, Lu J, et al. Fatigue life improvement of TC11 titanium alloy by novel electroshock treatment. Mater Des 2022;221:110902.
[18] Liu C, Xie L, Qian D, Hua L, Wang L, Zhang L-C. Microstructure evolution and mechanical property response of TC11 titanium alloy under electroshock treatment. Mater Des 2021;198:109322.
[19] Liu C, Yin F, Xie L, Qian D, Song Y, Wu W, et al. Evolution of grain boundary and texture in TC11 titanium alloy under electroshock treatment. J Alloys Compd 2022;904:163969.
[20] Xie L, Liu C, Song Y, Guo H, Wang Z, Hua L, et al. Evaluation of microstructure variation of TC11 alloy after electroshocking treatment. J Mater Res Technol 2020;9(2):2455–66.
[21] Bachmann F, Hielscher R, Schaeben H. Texture analysis with MTEX–free and open source software toolbox, Solid state phenomena. Trans Tech Publ; 2010. p. 63–8.
[22] Lehto P. Adaptive domain misorientation approach for the EBSD measurement of deformation induced dislocation substructures. Ultramicroscopy 2021;222:113203.
[23] Hielscher R, Silbermann CB, Schmidl E, Ihlemann J. Denoising of crystal orientation maps. J Appl Crystallogr 2019;52(5):984–96.
[24] Meng J-K, Liu L, Jiang J-T, Liao X-Q, Chen X-G, Zhen L. The role of biaxial stress ratio on the mechanical behavior and deformation mechanisms in HCP α-Ti. Mater Sci Eng, A 2023;862:144452.
[25] Gao J, Ben D, Yang H, Meng L, Ji H, Lian D, et al. Effects of electropulsing on the microstructure and microhardness of a selective laser melted Ti6Al4V alloy. J Alloys Compd 2021;875:160044.
[26] Ayad A, Ramoul M, Rollett A, Wagner F. Quantifying primary recrystallization from EBSD maps of partially recrystallized states of an IF steel. Mater Char 2021;171:110773.
[27] Gottstein G, Shvindlerman LS. Grain boundary migration in metals: thermodynamics, kinetics, applications. CRC press; 2009.
[28] Zhao Z, To S, Yip WS, Zhuang Z. A rapid method for grain growth of Ti6Al4V alloy and its machinability. Int J Adv Des Manuf Technol 2019;104:2347–61.
[29] Wang Z, Pu Q, Li Y, Xia P, Geng J, Li X, et al. Microstructures and mechanical properties of Al–Zn–Mg–Cu alloy with the combined addition of Ti and Zr. J Mater Res Technol 2023;22:747–61.
[30] Zhang L, Gu Y, Xiang Y. Energy of low angle grain boundaries based on continuum dislocation structure. Acta Mater 2017;126:11–24.
[31] Yang ZN, Jiang F, Wang XB, Qu L, Li YG, Chai LJ, et al. Effect of electropulsing treatment on microstructure and mechanical properties of a deformed ZrTiAlV alloy. Materials 2019;12(21):3560.
[32] Yeo T, Shigematsu N, Katori T. Dynamically recrystallized grains identified via the application of Gaussian mixture model to EBSD data. J Struct Geol 2023:104800.
[33] Zhao N, Sun Q, Pang Q, Hu Z. Comprehensive study of hot compression behaviors and microstructure evolution of solutionized 6082 aluminum alloy extruded bar. J Alloys Compd 2023;931:167541.
[34] Waryoba D, Islam Z, Reutzel T, Haque A. Electro-strengthening of the additively manufactured Ti–6Al–4V alloy. Mater Sci Eng, A 2020;798:140062.
[35] Han L, Jeurgens LP, Cancellieri C, Wang J, Xu Y, Huang Y, et al. Anomalous texture development induced by grain yielding anisotropy in Ni and Ni-Mo alloys. Acta Mater 2020;200:857–68.
[36] Salib M, Teixeira J, Germain L, Lamielle E, Gey N, Aeby-Gautier E. Influence of transformation temperature on microtexture formation associated with α precipitation at β grain boundaries in a β metastable titanium alloy. Acta Mater 2013;61(10):3758–68.
[37] Kannan R, Nandwana P. Texture evolution during processing and post-processing of maraging steel fabricated by laser powder bed fusion. Sci Rep 2022;12(1):6396.
[38] Konijnenberg PJ, Zaefferer S, Raabe D. Assessment of geometrically necessary dislocation levels derived by 3D EBSD. Acta Mater 2015;99:402–14.
[39] Gupta A, Khatirkar R, Singh J. A review of microstructure and texture evolution during plastic deformation and heat treatment of β-Ti alloys. J Alloys Compd 2022;899:163242.
[40] Antonysamy AA. Microstructure, texture and mechanical property evolution during additive manufacturing of Ti6Al4V alloy for aerospace applications. The University of Manchester (United Kingdom); 2012.
[41] Brandl E, Schoberth A, Leyens C. Morphology, microstructure, and hardness of titanium (Ti-6Al-4V) blocks deposited by wire-feed additive layer manufacturing (ALM). Mater Sci Eng, A 2012;532:295–307.
[42] Yan Z, Wang D, He X, Wang W, Zhang H, Dong P, et al. Deformation behaviors and cyclic strength assessment of AZ31B magnesium alloy based on steady ratcheting effect. Mater Sci Eng, A 2018;723:212–20.
[43] Wu B, Qiu Z, Dong B, Wexler D, Pan Z, Carpenter K, et al. Effects of synchronized magnetic arc oscillation on microstructure, texture, grain boundary and mechanical properties of wire arc additively manufactured Ti6Al4V alloy. Addit Manuf 2022;54:102723.
[44] Balasubramanian N, Langdon TG. The strength–grain size relationship in ultrafine-grained metals. Metall Mater Trans 2016;47:5827–38.
[45] Yu H, Yan M, Li J, Godbole A, Lu C, Tieu K, et al. Mechanical properties and microstructure of a Ti-6Al-4V alloy subjected to cold rolling, asymmetric rolling and asymmetric cryorolling. Mater Sci Eng, A 2018;710:10–6.
[46] Zhang S, Wang YC, Zhilyaev AP, Korznikova E, Li S, Raab GI, et al. Effect of grain size on compressive behaviour of titanium at different strain rates. Mater Sci Eng, A 2015;645:311–7.
[47] Long Y, Zhang W, Peng L, Peng H, Li X, Huang X. Mechanical behaviors of ultrafine-grained Ti-6Al-4V alloy during compression at various strain rates. Metall Mater Trans 2020;51(9):4765–76.
[48] Qu S, Zhai J, Sun P, Duan C, Li X. Influence of electropulsing assisted on machining properties of Ti-6Al-4V titanium alloy. Int J Adv Des Manuf Technol 2023:1–14.
[49] Xie L, Ren S, Yin F, Wang F, Qian D, Song Y, et al. Effects of three stress levels on the fatigue properties and fracture mechanisms of an in-situ synthesized TiB/Ti-6Al-4V titanium matrix composite. Mater Char 2023;195:112511.